HYDRAULIC-MECHANICAL CHARACTERISATION OF GEOTHERMAL RESERVOIR ROCKS

G. Blöcher[1], C. Kluge[1], T. Goense[2], L. Pei[3], R. R. Bakker[2], D.F. Bruhn[1,2]

[1] Helmholtz Centre Potsdam - GFZ German Research Centre for Geosciences

[2] TU Delft – CITG; Stevinweg 1; 2628 CN Delft, NL

[3] Wuhan Institute of Rock and Soil Mechanics, Xiaohongshan, 430071 Wuhan, P. R. China

guido.bloecher@gfz-potsdam.de

Keywords: physical rock properties, reservoir rocks, radial jet drilling

ABSTRACT

For the economic exploitation of geothermal reservoirs, the hydraulic transmissivity of the reservoir formation and therefore the reservoir productivity are key elements. In case of insufficient reservoir permeability or thickness, skin effects due to a transient chemical/mechanical alteration of the reservoir rock, the initial reservoir productivity could be low. To improve the overall well productivity, small laterals can be produced by high pressure water nozzles (jetted laterals) from the main well into the reservoir formation. Besides the increase of the drawdown area, even the bypassing of the wellbore skin can lead to an increase of the reservoir productivity. Moreover, the jettability of the reservoir rock strongly depends on the hydraulic and mechanical rock properties.

Various rock samples including samples from the major geothermal reservoirs in Europe were investigated. The samples include sandstone (e.g., Flechtinger sandstone, Gildehaus sandstone, Dortmunder sandstone), carbonates (e.g., Lower Carboniferous limestone), and rocks from volcanic regions (e.g., Odenwald granite, red interbasaltic sediments) from analogue outcrops. The samples were provided to measure hydraulic properties (porosity and permeability) as well as mechanical properties (Young's modulus, Poisson's ratio, tensile strength, uniaxial compressive strength, tri-axial compressive strength, cohesion, internal friction angle, and fracture toughness mode I).

Measurements of hydraulic and mechanical properties under saturated condition at elevated pressures will allow constructing constitutive relations for mechanical and hydraulic properties as functions of pressure and effective stress. Further, the 3D microstructure of rock samples was mapped using X-ray Computed Tomography (XCT) imaging technology and Electron Probe Micro-Analyser (EPMA) to characterise the rocks heterogeneity and to better understand the relative contributions of rock heterogeneity on (non-isothermal reactive) flow and mechanical properties of rock samples. The gained knowledge will be used to correlate the hydraulic and mechanical rock properties with the jettability of the reservoir rocks. Furthermore, the analysed measurements provide a useful database for further reservoir development and can be implemented as input parameters for various types of numerical simulations to understand and predict the long-term reservoir behaviour.

1. INTRODUCTION

Radial Jet Drilling (RJD) is a well stimulation technique that has drawn the attention of operators of geothermal doublets, mainly as a potential technique to improve the performance of the injector well. With radial jet drilling, several open hole laterals (typically 4 laterals per reservoir section) are jetted from the main well bore. Each lateral has a diameter between 25 mm and 50 mm and a length of maximum 100 m could be drilled. Orienting and jetting of one lateral will take 12 hours. The RJD will enhance the connectivity of the well to the rock and thereby the well productivity or injectivity. As with any stimulation technique, the suitability of radial jet drilling depends on the specific situation of the geothermal system. Although RJD is investigated and applied for Oil and Gas production, application for geothermal purposes are almost missing. Even more, radial jet drilling does not require large volumes of water to be applied and its application is more controlled than for example hydraulic fracturing, resulting in lower costs and less risk.

RJD shows highest efficiency in terms of performance increase in reservoirs with low permeability (< 10 mD). In contrast, the formation rock needs to have a minimum porosity of about 3-4% to be jettable. The most important criteria for the well are the minimum diameter (about 4 inch) and maximum along hole depth

(about 5 km). For tight gas reservoirs the gas production can be improved with a factor 4-7, simulation on geothermal cases show a potential performance increase by a factor of up to 3 when 8 laterals of 100 meter are successfully jetted and geological conditions are favourable.

In 2001 a study by (Buset et al., 2001) describes a new coiled tubing conveyed drilling technique suitable for both existing and new field developments. Besides reservoir permeability, skin effect, ratio between the vertical and horizontal permeability and oil viscosity, the self-induced nozzle pull force was considered to influence the jettability of the formation. (Buset et al., 2001) concluded as follows: The benefit of laterals increases with decreasing reservoir permeability and is most profound in reservoirs with high K_v/K_h ratios; penetrating the skin zones has big impact on total productivity; and best change in productivity is seen in high viscosity reservoirs.

An evaluation of radial drilling was performed by pilot tests in different shallow and deep oil field in Argentina (Bruni et al., 2007). The experiences show that detailed knowledge of the petrophysics, rock mechanics and pressure response are required.

The success of radial jet drilling was investigated (Abdel-Ghany et al., 2011) by use of numerical simulation and field tests. The maximum achieved increase of productivity was 173%. Besides these results the advantages and limitations of radial jetting technology were presented: (a) Porosity should be higher than 3-4%; (b) Maximum working depth about 3000 m; (c) Maximum tensile strength 690 MPa; (d) Maximum wellbore inclination 30 degrees; and (e) less than 120°C.

Is indicated above the jettability of porous media depends on both the hydraulic and the mechanical properties of the target rocks. Therefore, a comprehensive test program on various kind of potential geothermal reservoir rocks was performed to characterise their hydraulic and mechanical properties and to derive a linkage to their jettability.

2. MATERIALS

Several blocks were collected from various quarries, these include large samples (>50 x 50 x 50 cm) which were generally used for jetting tests, and smaller samples, used for thermal, hydraulic, mechanical, and chemical characterization. In some cases, core samples from the larger block samples were taken. Core samples were drilled using diamond-tip drill bits while flushed with water, and cut plan-parallel to the length required for the test using diamond-edge saw blades.

In general, if anisotropic features could be determined beforehand (from sample blocks), cores were drilled in certain directions are labelled with X, Y, or Z, where x and y directions are both along the bedding plane, z direction is perpendicular to bedding plane. For all samples (see Table 1), no further distinction between x and y directions is further made prior to drilling the samples, as no particular paleo-flow direction (or equivalent) could be determined from the individual blocks. It is therefore assumed that cores drilled in x and y directions are equivalent.

Table 1: Tested sedimentary, metamorphic and igneous rock types including their International Geo Sample Number (IGSN) and their project identifier ID.

Rock type	IGSN	ID
sedimantary rocks		
Ruhrsandstein	GFTRE0099	SRS6-DO
Bad Dürkheim sandstone	GFTRE0035	SBS6-BD
Roter Mainsandstein	GFTRE0091	SRM6-MI
Gildenhausener sandstone	GFTRE0065	SGH6-GI
Flechtinger sandstone		SBT6-BE
Oberkirschner sandstone	GFTRE0119	SWD6-OK
Friederwalder sandstone	GFTRE0057	SBS6-FR
Ruethener Gruensandstein	GFTRE0084	SRG6-RU
Interlayered sediments		VIB8-IC
Kohlenkalk	GFTRE0000	CKO6-AA
Massenkalk (Saurland)	GFTRE0014	CMA6-WU
metamorphic rocks		
Quartzite (Friedrichsdorf)	GFTRE0075	SQZ6-FR
igneous rocks		
Granite (Odenwald)	GFTRE0033	PGR6-RI
Iceland Basalt		VBA6-IC

3. METHODS

To assess the ability to produce a borehole with jet drilling technology, different thermal, hydraulic, and mechanical rock properties were measured on a suite of rock types. The thermal testing includes: thermal conductivity and effusivity; the hydraulic testing include: porosity and permeability measurements; and the mechanical testing include: Unixial Compresive Strength (UCS); Acoustic wave speeds (v_p & v_s, unconfined); triaxial deformation tests, tensile strength tests.

3.1. Thermal testing

Thermal conductivity (in W/mK) and effusivity (in $Ws^{0.5}/m^2K$) were determined using a C-Therm TCI Thermal Conductivity Analyzer, as installed at the Material Physics Lab, faculty of Aerospace Engineering, department of Aerospace Structures and Materials. For all samples, distilled water was used as contact fluid. As distilled water would move into pore space due to capillary effects, all measurements were conducted on saturated material.

3.2. Hydraulic testing - Porosity φ

First, porosity was determined using a helium pycnometer. Samples are flushed prior to pycnometer runs. In post-processing outliers are manually excluded

from averaging. The porosity is defined as the percentage of pore space, and is calculated as:

$$\varphi = \left(1 - \frac{V_{pyc}}{V_b}\right) \quad \textbf{(1)}$$

where V_{pyc} is the volume derived from the pycnometer (i.e., volume of grains) and V_{pyc} is the bulk volume of the sample (often a cylinder as the samples are subsequently used for other tests).

Second, the porosity and its distribution was analyzed by mercury porosimetry. In general, the capillary pressure is given by Laplace / Washburn Equation as follows:

$$p_c = p_a - p_w = \frac{2\gamma}{r_m} = \frac{2\gamma cos\theta}{R}, \quad \textbf{(2)}$$

with p_a - atmospheric pressure, p_w - hydrostatic pressure, p_c - equivalent pressure due to capillary forces, γ - surface tension, and θ - contact angle. Therefore, the capillary pressure can be linked to the pore radius.

Mercury intrusion porosimetry (MIP) is therefore an experimental technique used for the characterization of pore size distribution. By penetrating mercury into the pores of a specimen, the volume of penetrated pores diameter as a function of pressure is measured. The mercury volume that intrudes at each pressure increment, corresponds to the volume of pores of each size class. Since mercury is a non-wetting fluid, an externally imposed pressure is required to intrude the liquid into the pores of the rock sample. Besides the determination of the pore size distribution, the total porosity is determined from the total intruded volume mercury. It is measured by a mercury penetrometer (an electrical capacitance dilatometer) and has an accuracy of 0.1 μL.

Third, at the rock deformation laboratory of GFZ the porosity is measured by comparing the weight of the same core in oven-dry and saturated (distilled water) conditions. Using the weight difference and the density of distilled water the pore space is thereby calculated. Using this Archimedes principle, the sample will be weighted under dry conditions. Afterwards the sample is saturated and the weight of the saturated sample is measured. If the fluid density and the bulk volume of the sample are known, the porosity can be calculated as follows:

$$m_{Air} = m_s, \quad \textbf{(3)}$$

$$m_{Water} = m_s - V_s * \rho_f, \quad \textbf{(4)}$$

$$\rho_s = \frac{m_s}{V_s} = \frac{m_{Air} * \rho_f}{m_{Air} - m_{Water}}, \quad \textbf{(5)}$$

$$\varphi = \frac{V_b - V_s}{V_b} \quad \textbf{(6)}$$

with m_{Air}, m_{Water}, m_s – the mass in air, the mass in water and the mass of the solid phase, respectively. V_s and V_b denote the solid and bulk volume, and ρ_f and ρ_s the fluid and solid density.

3.3. Hydraulic testing - Permeability k

First, permeability k is measured inside a triaxial deformation vessel (Terratek) as installed in the rock mechanics laboratory of TU Delft, based on the principle of Darcy's law:

$$k = \frac{\dot{V}\mu L}{A\Delta P} \quad \textbf{(7)}$$

where $\dot{V}$ is the flowrate in m^3/s, μ is the viscosity of water at a certain temperature, in $Pa.s$, L is the sample length in meters, A is the cross sectional area in m^2 and ΔP is the pressure difference in Pascal.

Samples are radially confined using pressurized oil, separated by a rubber (EPDM) jacket. This type of jacket provides a good seal from low confining stress onward, preventing leakage between the sample wall and jacket. Axial confinement is brought to the sample by means of steel pistons and an axially applied load, measured with a load cell. These pistons have pore fluid lines embedded in them, and the end faces have grooves to allow equal distribution of fluid into the sample. Prior to measurements, samples are vacuumed, then flushed with CO_2, then flooded with distilled water. The distilled water is pressurized to dissolve any leftover CO_2, ensuring saturation.

Permeability measurements are conducted by flushing water through the sample at a known flowrate, and measuring the pressure difference across the sample. All measurements presented here are conducted with the constant flow method, using water at room temperature, at effective hydrostatic pressure and a pore pressure of 25 bar (regulated at outflow pump , i.e., backpressure). Flow rates are chosen such to limit the resulting pressure difference to less than 5% of the confining pressure. An example of a run at constant confining pressure, collecting 5 data points is shown in.

Errors in permeability are calculated as the result of machine precision for flowrate, measurement errors for length and diameter (corrected for changes due to confining pressure), and standard deviation of pressure difference within a certain time window where a constant flowrate is imposed.

Second, the permeability is determined in the triaxial press at GFZ based on Darcy's law. Here flow through experiments with distilled water are performed. The permeability is determined for all samples at a confining pressure of 2 MPa and a fixed outlet pressure p_{out} in the range of 0.1 to 0.2 MPa. Constant flow rates were in the order of 0.001 to 0.01 ml/min.

To quantify the effect of the effective pressure on the permeability, a constant flow is applied during the increase of confining pressure. The effective pressure is determined based on the effective pressure theory of (Terzaghi, 1936):

$$p_e = p_c - p_p \quad \textbf{(8)}$$

Where the mean pore pressure is assumed as:

$$p_p = p_{out} + 0.5(p_{in} - p_{out}) \quad \textbf{(9)}$$

Third, the gas permeameter (Pepe) at GFZ was used to determine the permeability. A cylindrical rock sample with a height of 40 or 50 mm and a diameter of 25 mm is put in a neoprene rubber jacket. Afterwards, the sample is placed in a hollow steel cylindrical chamber. Between the specimen and the threaded steel cylinder there is a space for hydraulic fluid to adjust the confining pressure. The recording frequency of the pressures and flow rates is 0.1 s^{-1}. By controlling the flow and setting a constant confining pressure of 5 MPa and an outlet pressure of ~0.15 MPa, the inlet pressure at the top of the sample is monitored over time. After achieving a constant inlet pressure at a certain flow rate, the flow rate is increased for the next step. In total four steps of different flow rates are performed to obtain the permeability. The intrinsic permeability is described by Darcy's law.

This equation only holds for liquid fluids. For the use of gas, there are mainly two complications: compressibility and gas slippage. Gas is a compressible fluid and the application of high pressure during the gas permeameter test causes compression. The modified flow equation for compressible fluids is expressed by:

$$\dot{V} = -A\frac{k_{gas}}{\mu L}\frac{p_{in}^2 - p_{out}^2}{2p_{out}}. \quad \textbf{(10)}$$

(Klinkenberg, 1941) discovered a higher gas permeability with respect to liquid permeability and attributed this to the slippage of gas molecules along grains. In comparison to a liquid, the average velocity of gas in the vicinity of pore walls is nonzero and therefore contributes to the flow. The Klinkenberg correction translates the gas permeability into the equivalent liquid permeability by:

$$k_{gas} = k_{liquid}\,(1 + \frac{b}{P}) \quad \textbf{(11)}$$

$$b = \frac{c\kappa T}{\pi\sqrt{2r^3}} \quad \textbf{(12)}$$

Where b is the Klinkenberg slip factor (Pa), P the average pressure of the sample (Pa), c a constant, T the temperature (K), r the sample radius and κ the Boltzmann's constant (JK^{-1}). For high pressures the liquid permeability is equal to the gas permeability if $2/(p_{in} + p_{out}) = 0$. Extrapolation of the k_{gas} is performed by linear extrapolation. Based on a maximum pressure difference of 5 MPa and a minimum measurable flowrate of 0.02 mL/min, this method can measure the permeability down to 10 nD.

3.4. Mechanical testing - Brazil disk indirect tensile strength / Fracture Toughness

Core samples cut to discs, with length equal to half of the radius of the samples were used. These were diametrically loaded by line loads using specially designed jogs (according to ASTM standards), assuming an effective angle of load of 10˚. Samples were deformed at a loading rate such that failure occurred within half a minute. To avoid high deformation rates during failure (overshoot), the machine was operated in constant displacement mode instead of loading rate. Moreover, by logging the load and displacement, fracture toughness could be determined using the method of (Guo et al., 1993).

For samples with clear anisotropic features (e.g., bedding, foliation) orientations of the discs with respect to the load direction have been taken into account. If no such information is available the sample is considered isotropic, and all data is used for averaging.

3.5. Mechanical testing - Young's' Modulus, Poisson's ratio, and Uniaxial Compressive Strength (UCS)

Samples with a length to diameter ratio of 2.5:1 were deformed at a constant displacement rate, such that the engineering strain rate was 10^{-5} s^{-1}. Axial displacement was logged using two linear variable differential transducers (LVDTs), and used to calculate axial strain by:

$$\varepsilon = \frac{\Delta l}{l_0} \quad \textbf{(13)}$$

where ε is the engineering strain, Δl the change in length of the sample, and l_0 the initial length of the sample. Axial LVDT's are placed around the sample, avoiding corrections for apparatus compliance. The samples were fitted with a chain-gap type LVDT to measure radial displacement. Load is measured with a load cell, and converted to axial stress by dividing to the initial cross sectional area normal to the load direction. As "barreling"-effects were limited (radial strain $< 1\%$), no corrections for increased cross sectional area were performed.

Elastic properties are determined by fitting axial stress vs axial strain as well as axial stress vs radial strain curves by a 1st order polynomial. Fit area is chosen such to limit influence of crack closure / machine settling at early stages of the experiment and also not to include the regime where subcritical crack growth is expected. The slope of the axial stress with axial strain is taken as Young's Modulus. Poisson's ratio is determined by dividing the negative of the Young's Modulus by the value of the slope of the axial stress with radial strain. This method was chosen instead of evaluating the lateral and axial strain at 50% of

maximum load, to avoid unrealistic high (axial) strain values due to crack closure and / or machine settling. Errors of the elastic properties are determined by using the associated errors of the linear regressions, determined by an alpha-95 prediction interval.

3.6. Mechanical testing - Triaxial compressive strength, Cohesion, and Internal friction angle

The Terratek apparatus described above is additionally used for tri-axial testing. Tests were either run room-dry, or under drained conditions, using constant back-pressure. The later also allows for monitoring of pore space destruction (pore collapse) or creation (microcracks). Radial strain is based on a chain-type LVDT similar to the UCS tests, corrected for (changing) jacket wall thickness during tests. Axial strain is determined using two LVDT's, mounted around the sample avoiding corrections for machine compliance. The Terratek apparatus is can handle maximum confining pressure up to 500 bar, and maximum axial load of 300 kN.

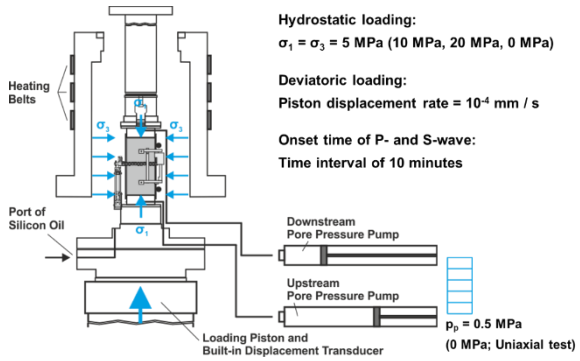

Figure 1: Mechanical Testing System (MTS 815) at GFZ used for tensile, uniaxial and tri-axial strength tests as well as some hydraulic tests.

At GFZ all tensile, uniaxial and tri-axial strength tests as well as some hydraulic tests were performed using the MTS 815 apparatus (Figure 1). This mechanical testing system (MTS) is a servo controlled compressive machine with 2000 kN vertical loading capacity. The apparatus consists of a stiff loading frame with a closed tri-axial cell, a set of independently operating Quizix 6000-Series pumps and a data-monitoring and acquisition system. In situ conditions can be simulated by hydrostatic pressures up to 140 MPa and temperatures up to 150 °C using oil as the confining medium. The axial strain and lateral strain of the core samples are measured by two Linear Variable Differential Transformers (LVDTs) and a circumferential chain extensometer, respectively. The resolution of the vertical and circular extensometer is $1 * 10^{-3}$ mm resulting in an axial strain resolution of $2 * 10^{-5}$ mm/mm and a lateral strain resolution of $1 * 10^{-6}$ mm/mm. The temperature is continuously monitored by two thermocouples, installed at the top and bottom of the specimen. Pore pressure is simulated by the use of two independent up- and downstream Quizix pumps. These pumps operate in constant pressure or constant flow rate mode and monitor accurately the volume change of the sample as a result of changing temperature or stress. The pressure difference over the sample is determined by a differential pressure sensor within the range of 0.01 to 1 MPa.

3.7. Mechanical testing – Acoustic wave velocity

Acoustic wave velocities are determined using a set of transducers designed for a peak response frequency of 1 MHz. A single sine wave pulse is sent from a sender each 10 ms, which is in turn picked up by the receiver. This is repeated for at least 50, and the data is stacked to filter out noise effects. Picking first arrival is done graphically using the waveform itself as well as by using the spectrogram. The latter is particularly useful when the influence arising from $v_s - v_p$ conversion is relatively high. As a result, time-picking errors are in the order of 0.1 µs.

3.8. Chemical testing - Mineral and chemical composition

Both mineral composition and chemical composition (major oxides) of samples was determined at the faculty of Mechanical, Maritime and Materials Engineering (3mE), Department of Materials Science and Engineering. Samples consist of pressed pills, made up from ground-up starting material (often saw-cuts that were not viable for mechanical testing).

For X-ray diffraction (XRD, mineral composition) the following instrument (and settings) was used: Bruker D8 Advance diffractometer Bragg-Brentano geometry with graphite monochromator and Vantec position sensitive detector. Co Kα radiation. Divergence slit 6M16 V12, scatter screen height 8 mm, 45 kV 35 mA. Sample spinning. Measurements were conducted with the following parameters: Coupled θ-2θ scan 10° -130°, step size 0.041° 2θ, counting time per step 1 s. Data evaluation is conducted using Bruker software Diffrac Suite, EVA vs 4.2.

Chemical composition (major oxides) was determined using: Panalytical Axios Max WD-XRF spectrometer. Data evaluation was done with SuperQ5.0i/Omnian software.

Furthermore, an electron probe microanalyzer (EPMA) is used to determine the mineral composition, grain size, grain geometry and microcrack structure. Within the EPMA, an electron beam is transmitted to the 30 µD thin sections. As a response, each element in the sample emits a characteristic X-ray which is detected by the electron microprobe. A high resolution image is generated which gives the opportunity to identify the textural structure on a micro scale level (1 µm). By the use of point analysis, the chemical composition of almost every single mineral can be determined. However, before conducting point analyses a standard should be used to calibrate the instrument. The analyses presented in this thesis are not point analyses but back-scatter detector (BSE) spectra where the intensity of

each single element is plotted in a spectrum. The resulting analyses will calculate the mineral composition norming all the oxides at 100%, not considering water which may occur in some mineral phases. The different minerals within the sample differ in their brightness related to the atomic weight of the elements forming the mineral. ImageJ software is used in order to estimate the mineral fraction of the thin sections.

4. RESULTS

The obtained results are exemplarily shown for the Kohlenkalk (CKO6-AA) a lower carboniferous limestone. All other results are summarized in Table 2.

4.1. Porosity and Pore Size Distribution

Two MIP experiments are performed to determine the porosity and pore size distribution. Two half cylindrical rock fragments are evaluated in terms of total mercury intrusion volume as a function of pressure. Figure 2 shows the raw data of the experiment. Both curves show an intrusion of ~0.4 mm³/g at around 0.1 bar. Mercury started to penetrate the pores of the CKO6-AA-MIP2 sample between 60 and 200 bar. Within the CKO6-AA-MIP1 the mercury intrusion started at around 200 bar, showing an exponential increase until a pressure of 2000 bar. Using the relation of (Washburn, 1921), the pore diameter distribution is obtained. The CKO6-AA-MIP1 shows a main pore diameter in the range of 0.01 – 0.05 µm, for the CKO6-AA-MIP2 a diameter of between 0.05 and 0.3 µm is found.

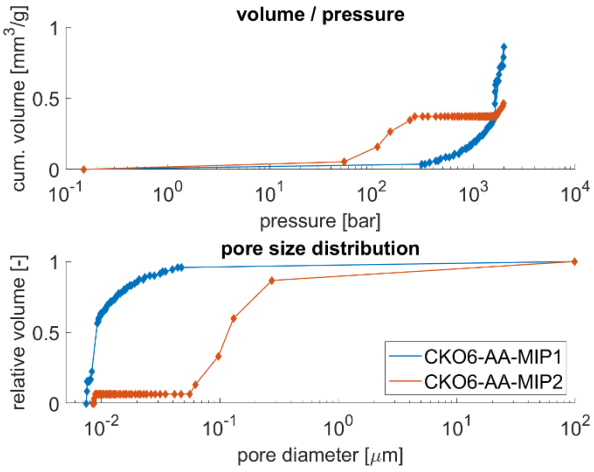

Figure 2: Mercury Intrusion Porosimetry (MIP) of two lower carboniferous limestone (Kohlenkalk) samples.

The porosity is determined by three different methods: Mercury Intrusion Porosimetry, Helium pycnometry and by the hydrostatic weighing method. All methods show porosity values between 0.21 and 1.00%, with a maximal uncertainty of +/- 0.88%. This uncertainty is mainly affected by measuring the sample dimensions (Helium pycnometer and dry/wet method). The MIP method is not dependent on the sample dimensions and is therefore the most accurate method, as indicated by the uncertainty range.

4.2. Permeability Measurements

By flow through experiments a clear distinction between the sample orientation and the permeability was obtained. In case the flow is parallel to the bedding, the permeability is ranging from 3 to 24 µD. In case the flow is parallel to the bedding the permeability is ranging from 47 to 154 µD. The minimum measurable permeability is about 1 µD.

Two rock samples are investigated at four different steady state flow rates with the gas-permeameter. The flow rate is kept constant for around 30 minutes in order to ensure a stable flow. The confining pressure is kept constant at 8 MPa for the duration of the entire experiment. Using Darcy's law and the Klinkenberg correction (Figure 3) a fluid permeability of 0.31 µD and 0.17 µD is obtained.

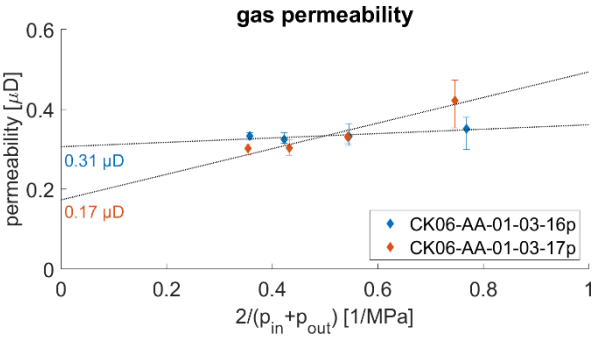

Figure 3: Permeability measurement of two lower carboniferous limestone (Kohlenkalk) samples obtained by gas permeameter.

4.3. Tensile Strength

The discs with their bedding orientation parallel to the vertical load show a tensile strength of 4.1 MPa. In the case of the other orientations, the load is perpendicular to the bedding. These samples show a tensile strength of 7.6 and 6.5 MPa, which is 2 times larger compared to the samples with the load parallel to the bedding (Figure 4).

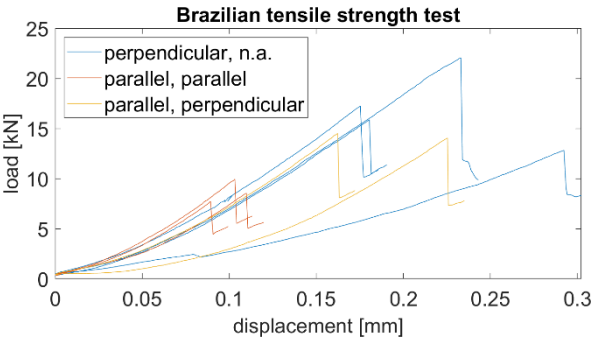

Figure 4: Brazilian tensile testing for samples cut perpendicular to bedding (blue) and parallel to bedding (load direction parallel (red) and perpendicular to bedding (yellow)).

4.4. Uniaxial compressive strength

Four unconfined UCS tests are performed, two on the xy-oriented and two on the z-oriented samples. The xy oriented samples showed a UCS of 116 MPa and 158 MPa, the z-oriented samples 124 MPa and 152 MPa. The stress - strain curves in Figure 5 are almost linear for all samples, indicating a fully elastic region until ultimate compressive failure.

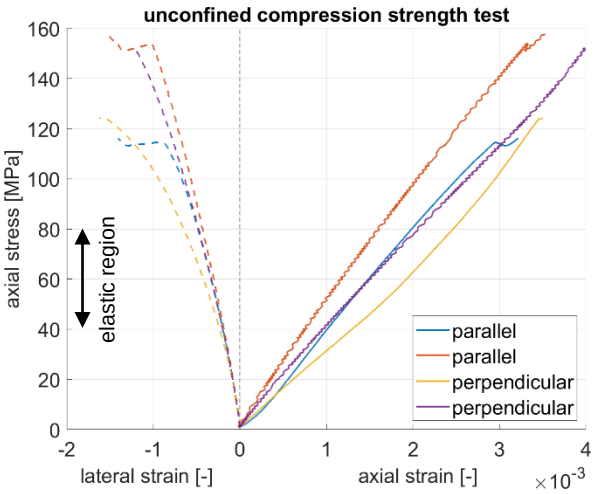

Figure 5: Unconfined Compression Strength (USC) test performed parallel and perpendicular to the bedding.

4.5. Triaxial testing

Tri-axial loading is performed with seven samples (Figure 6), at the confinement pressures of 20, 30, 40 and 50 MPa. The xy-oriented cores show a clear increase in compressive strength as the confining pressure increases. At the confining pressure of 20 MPa, the rock sample shows an UCS of 197 MPa which is significantly lower compared to the UCS of 306 MPa at 40 MPa. The z-oriented cores on the other hand show no significant difference as a function of the confining pressure. Their UCS is slightly increasing at a higher confining pressure, however, based on the differential pressure there is almost no increase in compressive strength. The samples with a confining pressure of 20 MPa show a different fracture structure in comparison to the tests performed at higher confining pressures. The CKO6-AA-01-03-06p has 3 main diagonal fractures and the CKO6-AA-01-02-01s one main fracture interrupted by a complex conjugate fracture structure. All samples with a confining pressure of at least 30 MPa showed one main diagonal shear fracture. During the axial loading, the axial and lateral strain were monitored by the extensometers.

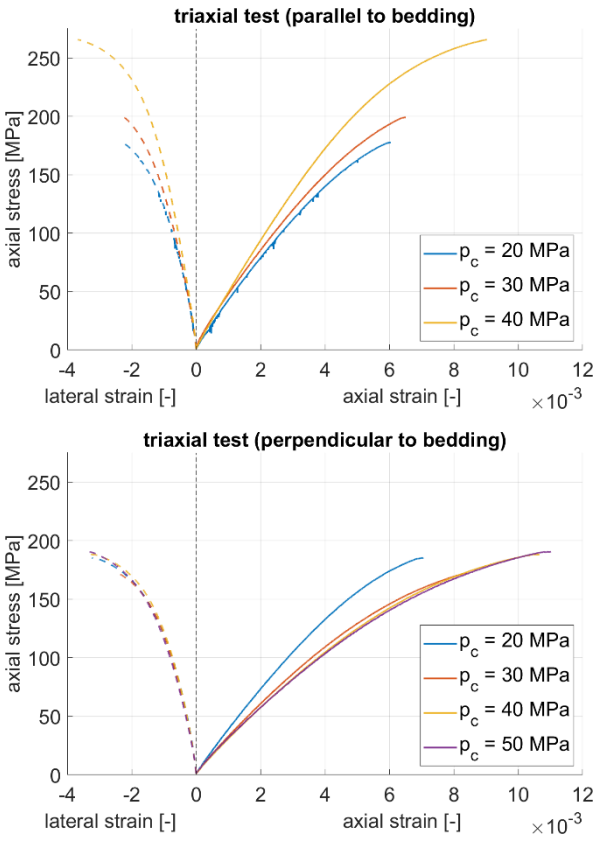

Figure 6. Triaxial testing with axial stress parallel to bedding (top) and perpendicular to bedding (bottom).

For the construction of the failure envelopes (Figure 7), a failure angle of 27° is assumed based on the measured failure angles of the deformed samples and a best fit of the failure envelope itself. A difference in the friction coefficient between the different orientations is clearly shown by failure envelopes. The friction coefficient of the parallel samples with 0.38 is significantly lower compared to a friction coefficient of 0.77 of the perpendicular samples. The cohesion of the xy-oriented and z-oriented rock samples are 46.4 MPa and 31.6 MPa, respectively.

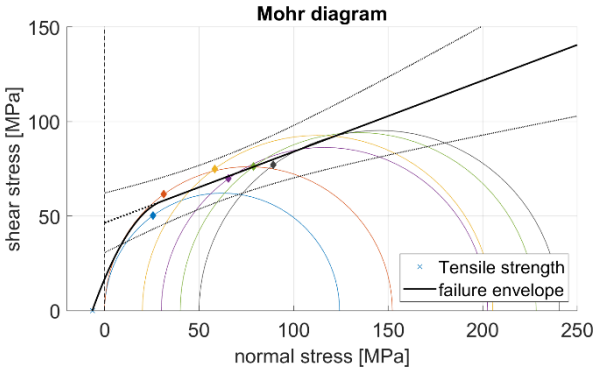

Figure 7: Mohr diagram for the xy-oriented rock samples.

4.6. Young's modulus and Poisson's ratio

Both the Poisson's ratio and Young's modulus are determined within the elastic region of the stress strain curve of both the unconfined and tri-axial compressive tests. Due to micro-crack closure of pre-existing cracks, the strain shows a non-linear behavior at vertical stresses below 25% of the failure strength. Plasticity starts to have an effect at vertical stresses of over 75% of the failure strength. The interval between the vertical stress of 40 MPa and 80 MPa is chosen, because the non-linear behavior of the rock is not affecting the determination of the elastic moduli (Figure 8).

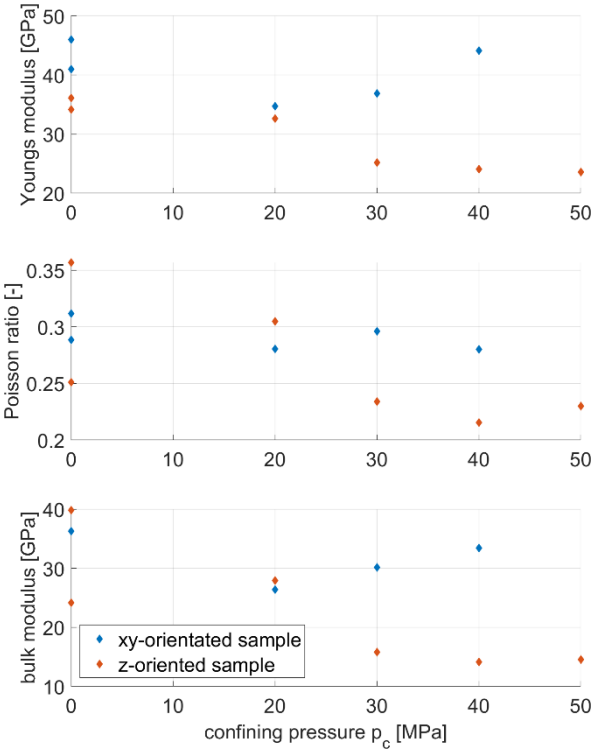

Figure 8: Young's modulus, Poisson ratio and bulk modulus of unconfined and tri-axial compressive tests.

5. DISCUSSION & CONCLUSIONS

A comprehensive dataset of thermal, hydraulic, mechanical and chemical properties of geothermal reservoir rocks were derived by laboratory experiments. The main focus is to characterize these reservoir rocks and to derive a linkage between the individual properties and the jettability of target formation. Therefore, some of the aforementioned rock types (Gildenhaus sandstone [SGH6-GI]; Kohlenkalk [CKO6-AA]; Bad Dürkheim sandstone [SBS6-BD]; Friederwalder sandstone [SBS6-FR]; Ruhrsandstein [SRS6-DO]; Interlayered sediments [VIB8-IC]) were used to investigate their jettability. The jetting treatment of the Gildenhaus sandstone and Interlayered sediments were most successful. Here a qualitative correlation could be made: the higher the porosity the higher the jettability. Note that Gildehaus sandstone is roughly 5 orders of magnitude more permeable than the interlayered sediments. However, both rock types were jettable at surface conditions. We therefore conclude that porosity does not necessarily need to be connected. Moreover, if the main operating mechanism behind jet drilling is pore-wall failure, a low permeability will better enable local high pore pressures (i.e., individual pores with high fluid pressure). However, a more detailed study on the micromechanics of jet technology is required to better test such hypothesis.

6. REFERENCES

Abdel-Ghany, M.A., Siso, S., Hassan, A.M., Pierpaolo, P., Roberto, C., 2011. New Technology Application, Radial Drilling Petrobel, First Well In Egypt, in: Offshore Mediterranean Conference and Exhibition, 23-25 March, Ravenna, Italy. Offshore Mediterranean Conference, p. .

Bruni, M.A., Biasotti, J.H., Salomone, G.D., 2007. Radial Drilling in Argentina, in: Latin American & Caribbean Petroleum Engineering Conference, 15-18 April, Buenos Aires, Argentina. Society of Petroleum Engineers, p. . https://doi.org/10.2118/107382-MS

Buset, P., Riiber, M., Eek, A., 2001. Jet Drilling Tool: Cost-Effective Lateral Drilling Technology for Enhanced Oil Recovery, in: SPE/ICoTA Coiled Tubing Roundtable, 7-8 March, Houston, Texas. Society of Petroleum Engineers, p. . https://doi.org/10.2118/68504-MS

Guo, H., Aziz, N.I., Schmidt, L.C., 1993. Rock fracture-toughness determination by the Brazilian test. Eng. Geol. 33, 177–188. https://doi.org/10.1016/0013-7952(93)90056-I

Klinkenberg, L.J., 1941. The Permeability Of Porous Media To Liquids And Gases. Drill. Prod. Pract.

Terzaghi, K., 1936. The shearing resistance of saturated soils and the angle between the planes of shear. First Int. Conf. soil Mech. 1936 1, 54–59.

Washburn, E.W., 1921. The Dynamics of Capillary Flow. Phys. Rev. 17, 273–283. https://doi.org/10.1103/PhysRev.17.273

7. ACKNOWLEDGEMENTS

The research for this paper received funding from the European Union's Horizon 2020 research and innovation programme under grant agreement No. 654662 (SURE). RB&DB thank: the TU Delft GSE lab laboratory staff for technical support; Ruud Hendrikx at the Department of Materials Science and Engineering at TU Delft is acknowledged for X-ray analysis; and Durga Mainila at the TU Delft faculty of Aerospace Engineering for his help with thermal property determination.

Table 2: Thermal, hydraulic, and mechanical properties of the tested rock samples.

IGSN	ID	Thermal Effusivity *e*	Thermal Conductivity *λ*	Porosity *φ*	Permeability *k*	Tensile strength *TS*	Fracture toughness *K1c*	Uniaxial Compressive Strength *UCS*	Young's modulus *E*	Poisson's ratio *ν*	Triaxial compressive strength	Cohesion *C*	Internal friction angle *μ*	Acoustic Wave Speeds v_p	Acoustic Wave Speeds v_{sh}	Acoustic Wave Speeds v_{sv}
		[$Ws^{1/2}/m^2K$]	[W/mK]	[-]	[m²]	[MPa]	[MPa $m^{1/2}$]	[MPa]	[GPa]	[-]	[MPa]	[MPa]	[°]	[km/s]	[km/s]	[km/s]
					xy/z/ab	xy/z/ab	xy/z/ab							xy/z/ab	xy/z/ab	xy/z/ab
sedimantary rocks																
GFTRE0099	SRS6-DO	2957	4.0	9.0		5.25/6.58/8.46	0.67/0.47/0.88	93.5-99.1	12.7-15.4	0.12-0.14	-	-	-	3.66/3.25/-	2.51/2.34/-	2.38/2.36/-
GFTRE0035	SBS6-BD	3087	4.3	19.0	3.0E-15/3.0E-16/-	-/-/2.46	-/-/0.23	22.5-34	4.8-7.3	0.21-0.26	-	8.65	28	2.95/2.96/-	1.95/1.99/-	-/-/-
GFTRE0091	SRM6-MI	2922	3.9	14.0	3.0E-15/1.0E-15/-	2.91/5.85/-	0.35/0.64/-	50.9-66.5	10.2-11.7	0.24-0.32	-	21.5	20.7	3.03/4.09/-	2.00/2.01/-	-/-/-
GFTRE0065	SGH6-GI	3233	4.6	24.0	-/-/2.3E-13	-/-/3.15	-/-/0.37	39-42	13.9-14.3	0.31-0.37	-	-	-	-/-/2.61	-/-/1.75	-/-/1.74
-	SBT6-BE	-	-	8.5	2.0E-16/-/-	-/-/3.82	-/-/0.48	56.45	14.9	0.285	σ3=(5,10,20); σ1=(94.7,126.3,179.7)	15.8	43.2	-/-/-	-/-/-	-/-/-
GFTRE0119	SWD6-OK	-	-	17.0	2.0E-15/-/-	-/-/-	-/-/-	63-75	13.7-15.6	0.21-0.33	σ3=(20); σ1=(151.5)	-	-	2.87/3.05/-	2.00/2.01/-	1.93/2.02/-
GFTRE0057	SBS6-FR	1569	1.3	18.6		-/-/3.7	-/-/-	42-60	8.3-9.8	0.17-0.25	-	-	-	2.63/2.50/-	1.75/1.71/-	1.73/1.71/-
GFTRE0084	SRG6-RU	-	-	25.0	4.0E-13/-/-	-/-/-	-/-/-	13.5	4.4-4.7	0.03	-	-	-	2.54/2.64/-	1.66/1.73/-	-/-/-
-	VIB8-IC	1971	2.0	22.5	-/-/1.6E-18**	-/-/8.0	-/-/0.71	58 - 68	9.3 - 11.4	0.15-0.20	σ3=(10,20); σ1=(108.1,135)	16.3	35.4	-/-/3.4	-/-/2.06	-/-/-
GFTRE0000	CKO6-AA	2633	3.3	0.8	2.0E-19**/2.0E-19**/-	8.7/14.3/15.3	0.5/0.8/1.1	116-158	34.2-46	0.25-0.36	σ3=(20,30,40); σ1=(197,229,306)	46.4	20.8	-/-/-	-/-/-	-/-/-
GFTRE0014	CMA6-WU	2723	3.5	2.3	-	-/-/10.98	-/-/1.18	137-152	66.5-66.8	0.25-0.29	-	46.2	24.7	-/-/6.41	-/-/3.38	-/-/3.38
metamorphic rocks																
GFTRE0075	SQZ6-FR	3781	6.0	0*	-	-/-/17.47	-/-/1.40	307	46.6-56.7	0.09-0.11	-	-	-	-/-/5.36	-/-/3.56	-/-/3.58
igneous rocks																
GFTRE0033	PGR6-RI	2444	2.9	0.6	-	-/-/11.85	-/-/1.35	120-142	39.9-47.6	0.19-0.26	-	-	-	-/-/4.77	-/-/3.06	-/-/2.85
-	VBA6-IC	2080	2.2	5.3	-/-/8.1E-18**	-/-/7.16	-/-/0.96	146-149	16.5-17.4	0.21-0.24	-	-	-	-/-/3.68	-/-/2.36	-/-/2.37

* below detection limit

** pulse decay method (gas permeameter)